



Landfalling tropical cyclones accelerate due to land–sea thermal and roughness contrasts

Received: 4 July 2024

Accepted: 26 November 2025

Published online: 27 January 2026

Check for updates

Quanjia Zhong^{1,2}, Johnny C. L. Chan^{1,3,4,5}✉, Wansuo Duan^{1,2}, Shifei Tu^{1,6}, Jianping Li^{7,8}, Jianping Gan^{1,9} & Ruiqiang Ding¹✉

Changes in the translation speed of landfalling tropical cyclones (TCs) pose great challenges in disaster preparedness. While some recent studies have discussed the increased chance of a reduction in the annual-mean translation speed of TCs after landfall, such changes before landfall have not been systematically investigated, especially for short-term variations (that is, hour-to-day timescales). Here we show, first based on observations, that globally, a TC about to make landfall tends to accelerate towards the coast, with an average acceleration of about 0.83 m s^{-1} per day, which means that the mean translation speed of a landfalling TC increases by ~48% during the 60-h period before landfall. Such an acceleration exists irrespective of TC intensity, seasonality and ocean basin, although its magnitude varies. Numerical simulations demonstrate that land–sea differences in surface roughness and thermal effect result in asymmetric circulation and convection in TCs, both of which are enhanced as the TC moves closer to the coast, leading to local changes in potential vorticity and thereby accelerating the storm. As this phenomenon is due to the land–sea contrast, a TC approaching the coast will probably have such an acceleration and hence it is inherent.

A tropical cyclone (TC) making landfall can bring about severe disasters due to its intense winds, heavy rain and storm surge^{1–3}. Recent studies have suggested that owing to global warming, a TC is likely to slow down, stalling the heavy rain associated with the TC after landfall and, hence, a greater chance of flooding^{4–6}. As disaster preparedness efforts need to be initiated well in advance, an accurate prediction of its position and timing of landfall is essential⁷. In particular, the translation speed of a TC is closely related to changes in its intensity⁸, rain rate⁹ and rainfall area¹⁰. It is therefore important to know whether the TC

translation speed will change before landfall. Most previous studies have primarily focused on examining the long-term change (that is, interannual and interdecadal variability) in the annual-mean speed of TCs^{11–13}. However, so far, no systematic study has been made on the short-term (that is, hour-to-day timescales) variations in the speed of individual TCs, particularly when each of them is about to make landfall. Here we show, using both observational data and numerical simulations, that owing to the differences in friction and thermal effects between land and sea, TCs approaching a coastline have an

¹State Key Laboratory of Earth Surface Processes and Disaster Risk Reduction, Beijing Normal University, Beijing, China. ²State Key Laboratory of Earth System Numerical Modeling and Application, Institute of Atmospheric Physics, Chinese Academy of Sciences, Beijing, China. ³Asia-Pacific Typhoon Collaborative Research Center, Shanghai, China. ⁴Shanghai Typhoon Institute, China Meteorological Administration, Shanghai, China. ⁵School of Energy and Environment, City University of Hong Kong, Hong Kong, China. ⁶South China Sea Institute of Marine Meteorology, College of Ocean and Meteorology, Guangdong Ocean University, Zhanjiang, China. ⁷Frontiers Science Center for Deep Ocean Multi-spheres and Earth System/Key Laboratory of Physical Oceanography/Academy of Future Ocean/College of Oceanic and Atmospheric Sciences, Center for Ocean Carbon Neutrality, Ocean University of China, Qingdao, China. ⁸Laboratory for Ocean Dynamics and Climate, Qingdao Marine Science and Technology Center, Qingdao, China. ⁹Center for Ocean Research in Hong Kong and Macau and Department of Ocean Science, Hong Kong University of Science and Technology, Hong Kong, China. ✉e-mail: Johnny.chan@cityu.edu.hk; drq@bnu.edu.cn

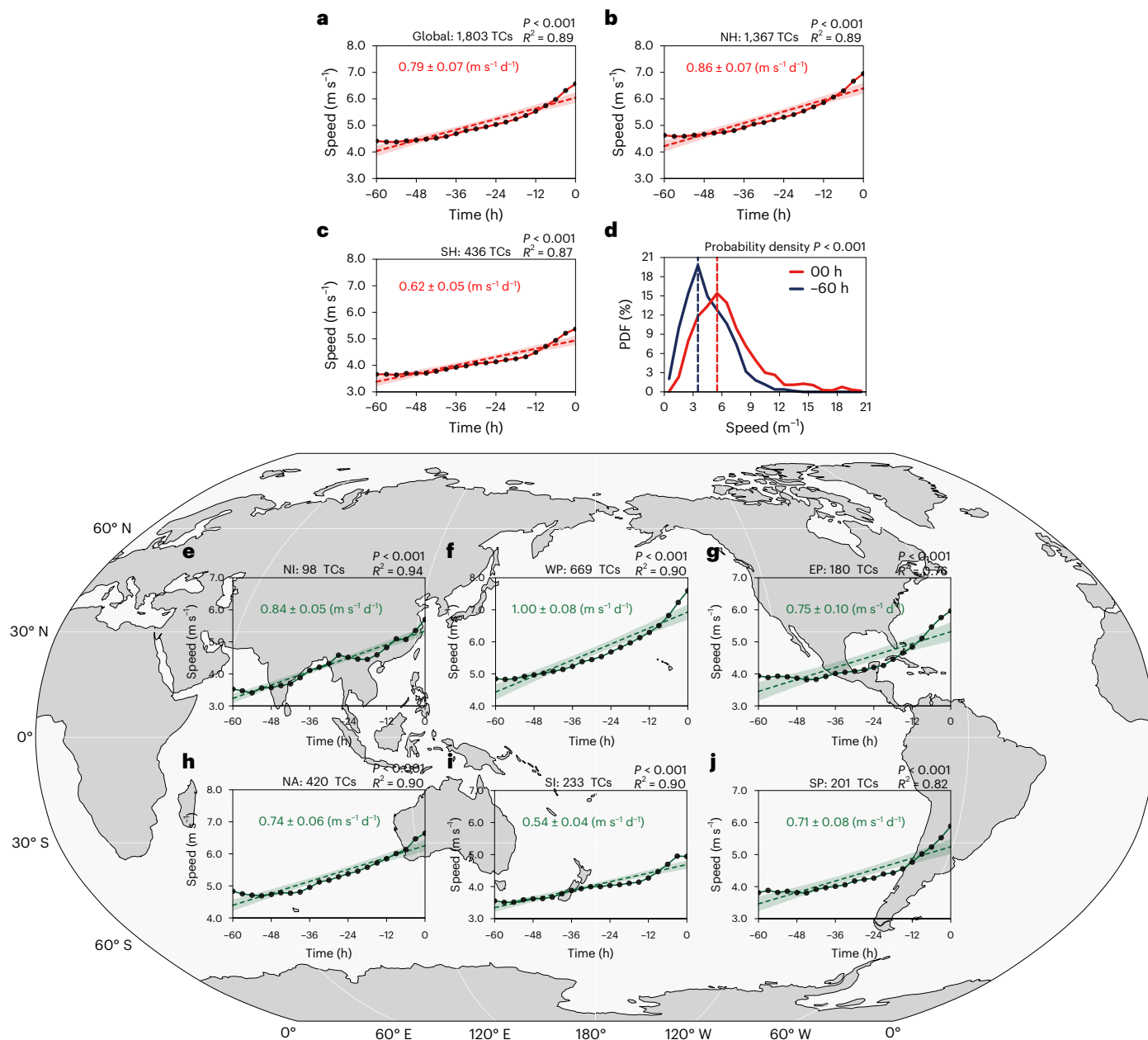


Fig. 1 | Changes in translation speed of landfalling TCs. **a–c**, The changes in the translation speed of landfalling TCs globally (**a**), in the Northern Hemisphere (NH) (**b**) and in the Southern Hemisphere (SH) (**c**). **d**, The probability distributions (%) of translation speed 60 h before landfall (blue) and at landfall (red). The dashed lines mark the maximum probabilities. **e–j**, The changes in the translation speed of landfalling TCs in North Indian (NI) (**e**), the Western North Pacific (WP) (**f**), the Eastern North Pacific (EP) (**g**), the North Atlantic (NA) (**h**), South Indian (SI) (**i**) and the South Pacific (SP) (**j**). The global mean translation

speed from 60 h before landfall to landfall is shown at 3-h intervals (solid line with dots), together with linear trends (dashed lines) and their 95% confidence intervals (shading). Statistical significance of the linear trends was assessed using a Student's *t*-test. Regression coefficients (in metres per second per day) with corresponding standard errors are shown, and *P* values and *R*² values are provided. The maps in panels **e–j** were generated using Python with publicly available coastline data from Natural Earth.

inherent tendency to accelerate towards the coast, irrespective of ocean basin, seasonality and intensity. This finding provides new insights into the physical processes influencing TCs acceleration near coastlines, which may help refine numerical models for trajectory prediction before landfall.

Global increase in translation speed of landfalling TCs

We begin by presenting analyses, using the available best-track data-sets, of all TCs making landfall along the various coastlines of all ocean basins around the world (for a detailed description of how the

landfalling TCs are selected, see Methods). It can be seen from Fig. 1a that, globally, the average speed of a TC increases as it approaches the coastline. During the 60-h period before landfall, the mean translation speed of global landfalling TCs rises by 49.79%, with an associated rate of increase of $0.79 \pm 0.07 \text{ m s}^{-1} \text{ d}^{-1}$ (Extended Data Table 1). The acceleration in the Northern and Southern Hemispheres are $0.86 \pm 0.07 \text{ m s}^{-1} \text{ d}^{-1}$ (Fig. 1b) and $0.62 \pm 0.05 \text{ m s}^{-1} \text{ d}^{-1}$, respectively (Fig. 1c). The probability distribution of global mean translation speed also shows a clear shift towards higher speeds at the landfall time compared with 60 h before landfall (Fig. 1d). The difference in mean speed between the two distributions is statistically significant. Translation speeds of $< 4 \text{ m s}^{-1}$ are

more prevalent 60 h before landfall, while speeds of $>5 \text{ m s}^{-1}$ occur with higher probability at landfall.

To ascertain the effect of land, we further compared the 60-h changes in the translation speed of landfalling TCs before crossing the real coastline with that of non-landfalling TCs crossing an imaginary coastline shifted eastwards 800 km from the real coastline. The acceleration of landfalling TCs is generally greater than that of non-landfalling TCs ($0.79 \pm 0.07 \text{ m s}^{-1} \text{ d}^{-1}$ versus $0.60 \pm 0.02 \text{ m s}^{-1} \text{ d}^{-1}$), with a mean difference of $0.19 \text{ m s}^{-1} \text{ d}^{-1}$. These results demonstrate that landfalling TCs do have an extra acceleration, accounting for about 24% of their total acceleration, which can be attributed to the land–sea contrast.

To examine the effect of inhomogeneous TC datasets due to the change of observation methods in recent decades, we further break up all TCs records into the pre-satellite (1950–1979) and post-satellite (1980–2021) eras. The results show that both periods exhibit highly significant increasing trends of TC translation speed before landfall (Extended Data Table 1 and Extended Data Fig. 2a–c). The increasing translation speed for TCs is comparable between the post-satellite era and the pre-satellite era, with values of $0.81 \pm 0.07 \text{ m s}^{-1} \text{ d}^{-1}$ and $0.78 \pm 0.07 \text{ m s}^{-1} \text{ d}^{-1}$, respectively. These results indicate that the speed-up phenomenon of landfalling TCs does not depend on the reliability of the observational data.

All these results suggest that a TC tends to accelerate as it moves closer to the coastal areas until it makes landfall. TC acceleration poses a great challenge in forecasting not only on the timing of the landfall location but also on local rainfall and storm surge. The latter is especially important because the TC rain rate and intensity increase significantly with translation speed^{8,9}.

Acceleration exists irrespective of TC characteristics

The speed up of TCs before landfall is found in every basin; however, the basin-averaged rate of increase in the translation speed varies considerably in different ocean basins. For instance, the Northern Indian Ocean exhibits the largest acceleration, followed by the western and eastern North Pacific, Southern Pacific and North Atlantic, while the Southern Indian Ocean shows the smallest increase in the translation speed of TCs (Fig. 1e–g and Extended Data Table 1).

As TC activity exhibits distinct seasonal locking characteristics¹⁴, with more TCs in the summer and autumn, the seasonality of changes in translation speed of TCs is also examined based on their landfall time (Extended Data Fig. 2d–g and Extended Data Table 2). TCs across all seasons exhibit a speed-up tendency. Overall, the acceleration of landfalling TCs during transitional seasons (for example, spring and autumn) is greater than during the summer and winter.

The changes in translation speed for each of the TC intensity categories were also examined (for a detailed classification of intensity, see Methods). TCs in all categories (the intensity category of a particular TC is the highest intensity of the TC during the 60-h period) also exhibit a speed-up tendency (Extended Data Fig. 2h–m and Extended Data Table 1). The largest speed-up tendency is observed in category 3 TCs, while category 5 TCs show the smallest increase rate in the translation speed. Overall, the speed up before landfall does not depend on intensity, although the magnitude of acceleration varies in different intensity categories.

To summarize, these results demonstrate a very important phenomenon: as a TC moves close to a coastline and finally makes landfall, it will probably accelerate, irrespective of seasonality, intensity or coastal region. This can therefore be considered as an inherent property of landfalling TCs.

Role of land–sea contrast in the acceleration of TCs

To investigate the physics behind this inherent property of landfalling TCs, we perform a numerical simulation and adopt the potential

vorticity (PV) tendency (PVT) analysis approach^{15–17} (Methods). Here, we hypothesize that the acceleration effect of the landfalling TC is associated with asymmetric convection, primarily triggered by the land–sea contrast. This acceleration effect is similar to, and as important as, another inherent effect observed in all TCs—the beta effect^{18,19} induced by the earth's rotation—which is also difficult to identify in individual TCs because of the steering flow controlling TC movement. Indeed, the acceleration effect resulting from the land–sea contrast will become particularly important in situations of weak steering flow and without any other forcing mechanisms. Therefore, we performed an idealized numerical simulation with a very weak steering flow (for example, 1 m s^{-1}) so that this inherent effect is the dominant factor. Imposing a stronger steering flow could result in a large PV advection term, potentially masking this inherent effect. This will be discussed in more detail later.

The numerical simulation shows that the simulated TC indeed increases its speed as it moves closer to the land, with the speed increasing from 1.2 m s^{-1} to 1.6 m s^{-1} by the time the vortex reaches the coast (Fig. 2a,b). The acceleration of the simulated TC is $0.21 \text{ m s}^{-1} \text{ d}^{-1}$, which is comparable to the observed acceleration difference of $0.19 \text{ m s}^{-1} \text{ d}^{-1}$ between global landfalling and non-landfalling TCs (Extended Data Table 1). This confirms the robustness of the observational results from a numerical simulation perspective.

A diagnostic analysis of the PVT reveals that the increasing trend of PVT speed at a height of 1 km is consistent with the location speed trend, which is calculated based on the centre location of the simulated TC. The PVT vector points towards the west–southwest and its magnitude increases as the vortex moves closer to the land (Fig. 3). The same analysis using the averaged values of the PVT vector at 3–10 km height shows similar results (Extended Data Fig. 3), although, as expected, the contributions from individual terms in the PVT equation are different.

As vertical motion and asymmetric flow vary with height, the contributions of individual terms in the averaged PVT vector within the 3–10 km height range may not fully represent the vertically averaged field. A further analysis of the various terms in the PVT at a height of 1 km was therefore used to reveal the physical mechanisms behind the acceleration of landfalling TCs. When a TC moves closer to land, the land–sea roughness difference and thermal contrast would lead to a change in the vortex circulation, which generates an asymmetric flow as well as an asymmetric convection associated with the vortex (Extended Data Fig. 4). The combination of the asymmetric flow and the steering flow produces an asymmetric advection of symmetric PV (AASPV)²⁰, with the strongest advection occurring towards the northwest (Extended Data Fig. 5a). In addition, the asymmetric PV associated with the asymmetric convection is advected by the symmetric flow associated with the TC, which generates a symmetric advection of asymmetric PV (SAAPV)²¹ (Extended Data Fig. 5b). The sum of AASPV and SAAPV gives a northwestwards-pointing horizontal advection (HA) vector of PVT (Fig. 3).

Meanwhile, the asymmetric convection generates three heating-gradient components; the vertical component has the greatest magnitude, while the two horizontal components are much weaker (Extended Data Fig. 6). The vertical component of the heating gradient arises mainly from latent heat release associated with asymmetric convection located on the offshore side of the vortex circulation (Extended Data Fig. 4), which has been previously observed²² as well as numerically simulated²³. The sum of the three terms in the diabatic heating (DH) equation produces a DH vector, the magnitude of which also increases as the vortex moves closer to the land.

Overall, the main contributors to the increase of PVT are HA and DH, and the contribution of vertical advection (VA) to PVT is relatively small as the vortex moves closer to the land (Fig. 3). The same analysis using the averaged values of various HA, VA and DH within 3–10 km height shows similar results, although the contributions of the individual terms are different (Extended Data Fig. 3). This

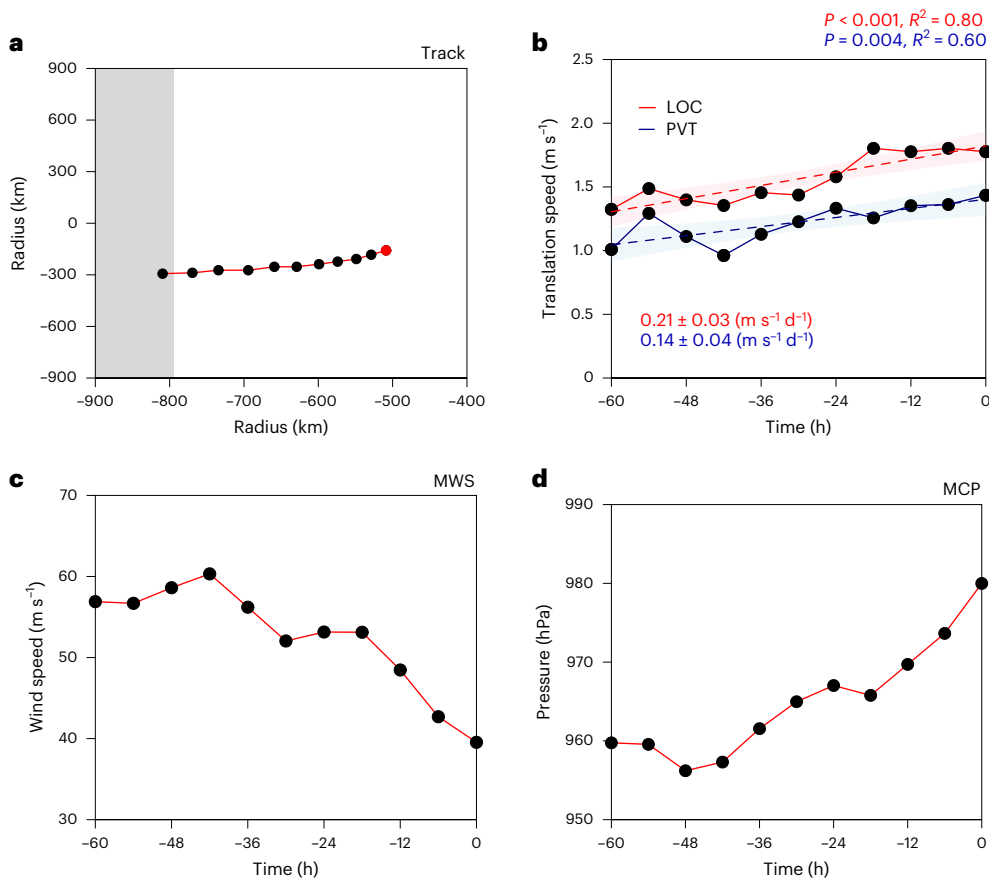


Fig. 2 | Track, translation speed, MWS and MCP of the simulated TC. **a**, The track of the simulated TC. The starting point (red dot) marks the TC location 60 h before landfall. **b**, The translation speed of the simulated TC. The solid blue and red lines show PVT speed and location (LOC) translation speed, respectively, calculated from centre positions at 1 km height (PVT) and at the surface (LOC).

The dashed lines denote the linear regression fits and shading indicates the two-sided 95% confidence intervals of the trend based on a Student's *t*-test. The regression coefficients with their standard errors (in metres per second per day) are shown, and the corresponding *P* values and R^2 values are provided. **c,d**, The MWS (**c**) and MCP (**d**) of the simulated TC.

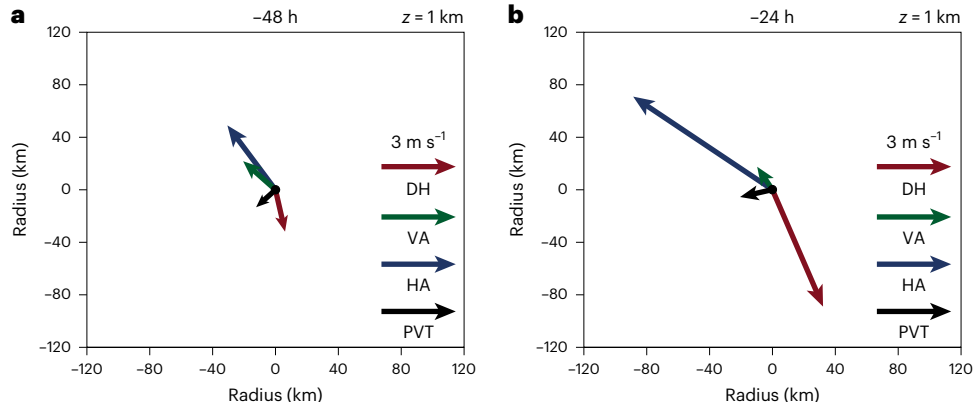


Fig. 3 | PVT vector and its various components. **a,b**, The PVT speed (black) at 1 km height and its contributions from HA (blue), VA (green) and DH (red) at 48 h (−48 h) (**a**) and 24 h (−24 h) (**b**) before landfall. The magnitude of the reference vector is 3 m s^{-1} .

situation is somewhat similar to that in which the asymmetric flow differs at each vertical level, but vertical averaging ultimately yields the steering flow^{24,25}.

A schematic diagram showing the various processes involved is shown in Fig. 4. The analyses presented here demonstrate that the land–sea differences in surface roughness and thermal effect lead to a change in the vortex circulation, which generates an asymmetric flow as well as asymmetric convection associated with the vortex. Such

asymmetries then lead to changes in the PVT to cause an acceleration of the vortex towards land. This simple experiment demonstrates that such an acceleration is an ‘inherent’ property of any TC-like vortex that moves towards an area of differential surface properties (roughness and thermal effect).

This study highlights a key aspect of TC movement during coastal approach: globally, landfalling TCs show an overall tendency to accelerate as they near the coast—an intrinsic behaviour that has not been

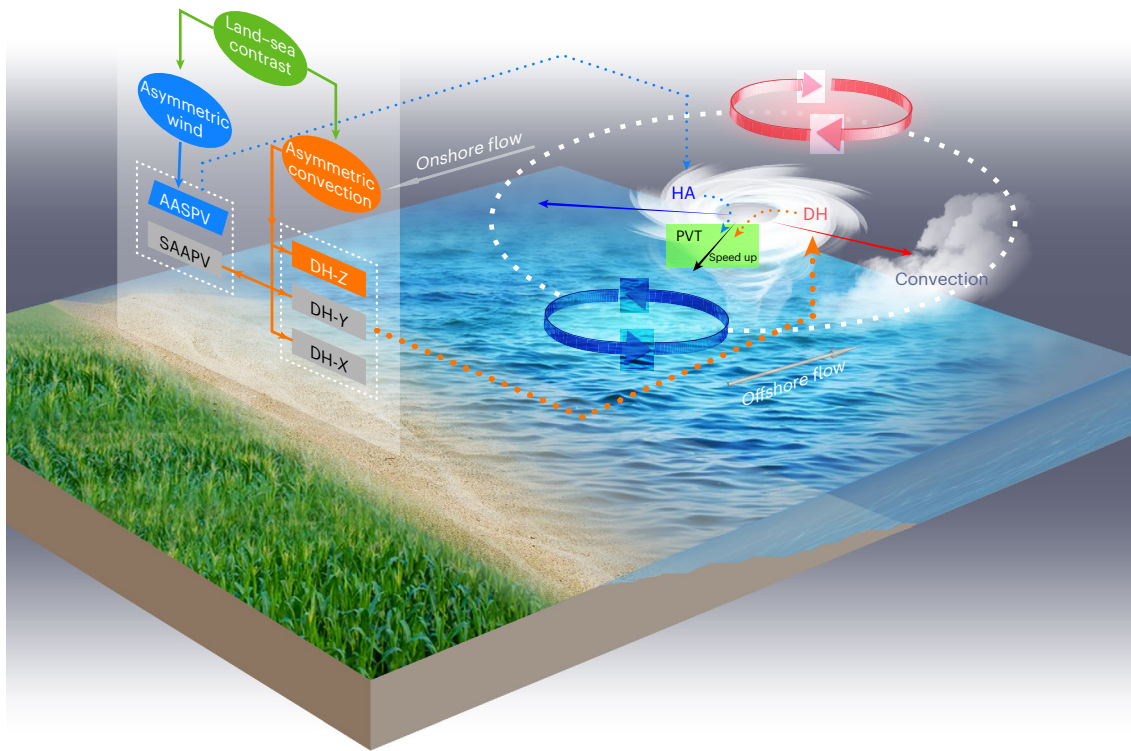


Fig. 4 | Schematic diagram of the physical mechanisms for the acceleration of landfalling TCs. The white spiral and dashed circle show a simplified TC structure in the Northern Hemisphere and its vortex circulation. The black, red and blue vectors denote PVT at 1 km and the contributions from HA and DH, respectively. The blue and pink curved arrows mark the asymmetric wind flows driving HA, while the cloud indicates offshore convection enhancing DH. The offshore and onshore flows are shown. HA is divided into AASPV and SAAPV. The DH gradients are labelled DH-X, DH-Y and DH-Z.

respectively. The blue and pink curved arrows mark the asymmetric wind flows driving HA, while the cloud indicates offshore convection enhancing DH. The offshore and onshore flows are shown. HA is divided into AASPV and SAAPV. The DH gradients are labelled DH-X, DH-Y and DH-Z.

recognized before. Of course, for a specific TC, many factors such as steering flow²⁶, vertical wind shear²⁷, topography^{24,25}, intensity changes⁸ and Coriolis force¹⁸ can also cause it to change speed, deflect or loop, which can supersede this intrinsic acceleration effect.

In addition to simulating the TC under weak steering flow, we also performed a simulation with a stronger steering flow, close to the usual translation speed (for example, 5 m s^{-1}), and found that the simulated TC also accelerates as it approached the coastline (Extended Data Fig. 7a). However, no acceleration of a TC is evident without the presence of land in the simulation (Extended Data Fig. 7b). Given that local circulations induced by thermal differences between land and sea (such as land-sea breeze circulations) may affect the development and movement of TCs, simulations with and without the radiative effect were also performed. The results show that without the radiative effect, the acceleration of TCs is weakened (Extended Data Fig. 7a,c). TCs experiencing periods of intensification or weakening both demonstrate acceleration near the coast. This suggests that the acceleration induced by land-sea differential friction and thermal contrasts is a robust feature, independent of the TCs' intensity change or translational speed.

The analyses presented here suggest that such an acceleration is a result of the differences in roughness and thermal effect between land and sea. In fact, globally, land-surface properties vary substantially by coastal region. Therefore, a numerical weather prediction model used to predict TC movement must incorporate realistic representations of the land surface to properly account for differences in surface roughness and thermal properties. Au-Yeung and Chan²⁸ have shown that as a vortex approaches land with different roughness, the vortex tends to move towards the area with higher roughness and hence the acceleration will be different. This is becoming more important as more

coastal areas are highly urbanized, which increases roughness, causing thermal contrast to also increase.

Over the past 50 years, TCs have claimed the lives of 779,324 people and resulted in a total direct economic loss of US \$1.4 trillion²⁹. The significance of this is study can be seen in landfalling TCs along the South China coast, a major hot spot for TCs in China, with an annual average of six to seven landfalling TCs³⁰. Along this coastline lies the Pearl River Delta, home to a mega-city cluster including Hong Kong, Macao and Guangzhou, among others, with a population exceeding 30 million. In 2018, damages in Hong Kong alone due to Supertyphoon Mangkhut amounted to US \$120 million³¹. This was one of the strongest TCs that has accelerated towards the southern coastal region of China³². If a numerical weather prediction model does not have an accurate representation of the land-surface properties within such a vast mega-city cluster, the prediction of the acceleration of a landfalling TC may be compromised, even if the synoptic flow patterns and TC characteristics are correctly predicted. This can lead to erroneous forecasts regarding the timing and location of landfall. With the time of TC landfall being advanced owing to its acceleration towards the coast, there might not be enough time to adequately prepare for storm surges, clearing drainage systems in anticipation of heavy rain or securing structures from potential wind damage, and hence the damage could be much more severe.

In addition to the global acceleration of landfalling TCs identified here, there is evidence that the rain rate of global TCs significantly increases with translation speed⁹. Furthermore, the mean intensity of a TC increases notably when its translation speed is slower than 5 m s^{-1} , while the area of TC rainfall expands as the potential intensity and size increase^{8,33}. Of particular relevance here is that the rainfall

accumulation of landfalling TCs within any given time frame will increase. This has a important impact on the exposure to TC-related hazards before landfall. Future studies that focus on short-term variations in the rain rate of landfalling TCs are also warranted.

Online content

Any methods, additional references, Nature Portfolio reporting summaries, source data, extended data, supplementary information, acknowledgements, peer review information; details of author contributions and competing interests; and statements of data and code availability are available at <https://doi.org/10.1038/s41561-025-01891-1>.

References

1. Zhang, Q., Wu, L. & Liu, Q. Tropical cyclone damages in China 1983–2006. *Bull. Am. Meteorol. Soc.* **90**, 489–496 (2009).
2. Needham, H. F., Keim, B. D. & Sathiaraj, D. A review of tropical cyclone-generated storm surges: global data sources, observations, and impacts. *Rev. Geophys.* **53**, 545–591 (2015).
3. Chen, L., Li, Y. & Cheng, Z. An overview of research and forecasting on rainfall associated with landfalling tropical cyclones. *Adv. Atmos. Sci.* **27**, 967–976 (2010).
4. Kossin, J. P. A global slowdown of tropical-cyclone translation speed. *Nature* **558**, 104–107 (2018).
5. Lai, Y. et al. Greater flood risks in response to slowdown of tropical cyclones over the coast of China. *Proc. Natl Acad. Sci. USA* **117**, 14751–14755 (2020).
6. Wu, K., Wang, C., Wu, L., Zhao, H. & Cao, J. Slowdown in landfalling tropical cyclone motion in South China. *Geophys. Res. Lett.* **49**, e2022GL100428 (2022).
7. Leroux, M.-D. et al. Recent advances in research and forecasting of tropical cyclone track, intensity, and structure at landfall. *Trop. Cyclone Res. Rev.* **7**, 85–105 (2018).
8. Mei, W., Pasquero, C. & Primeau, F. The effect of translation speed upon the intensity of tropical cyclones over the tropical ocean. *Geophys. Res. Lett.* **39**, L07801 (2012).
9. Tu, S. et al. Increase in tropical cyclone rain rate with translation speed. *Nat. Commun.* **13**, 7325 (2022).
10. Qin, L. et al. Global expansion of tropical cyclone precipitation footprint. *Nat. Commun.* **15**, 4824 (2024).
11. Wang, C., Wu, L., Zhao, H., Liu, Q. & Wang, J. An abrupt slowdown of late season tropical cyclone over the Western North Pacific in the early 1980s. *J. Meteorol. Soc. Jpn* **99**, 1413–1422 (2021).
12. Zhu, Y.-J. & Collins, J. M. in *Hurricane Risk in a Changing Climate* (eds Collins, J. M. & Done, J. M.) 43–56 (Springer, 2022).
13. Yamaguchi, M., Chan, J. C. L., Moon, I.-J., Yoshida, K. & Mizuta, R. Global warming changes tropical cyclone translation speed. *Nat. Commun.* **11**, 47 (2020).
14. Trepanier, J. C., Nielsen-Gammon, J., Brown, V. M., Thompson, D. T. & Keim, B. D. Stalling North Atlantic tropical cyclones. *J. Appl. Meteor. Climatol.* **63**, 1409–1426 (2024).
15. Wu, L. G. & Wang, B. A potential vorticity tendency diagnostic approach for tropical cyclone motion. *Mon. Weather Rev.* **128**, 1899–1911 (2000).
16. Fovell, R. G. et al. Influence of cloud microphysics and radiation on tropical cyclone structure and motion. *Meteorol. Monogr.* **56**, 11.11–11.27 (2016).
17. Fovell, R. G., Corbosiero, K. L., Seifert, A. & Liou, K. N. Impact of cloud-radiative processes on hurricane track. *Geophys. Res. Lett.* **37**, L07808 (2010).
18. Wang, B. & Li, X. The beta drift of three-dimensional vortices: a numerical study. *Mon. Weather Rev.* **120**, 579–593 (1992).
19. Chan, J. C. L. & Williams, R. T. Analytical and numerical studies of the beta-effect in tropical cyclone motion. 1. Zero mean flow. *J. Atmos. Sci.* **44**, 1257–1265 (1987).
20. Wong, M. L. M. & Chan, J. C. L. Tropical cyclone motion in response to land surface friction. *J. Atmos. Sci.* **63**, 1324–1337 (2006).
21. Chan, J. C. L., Ko, F. M. F. & Lei, Y. M. Relationship between potential vorticity tendency and tropical cyclone motion. *J. Atmos. Sci.* **59**, 1317–1336 (2002).
22. Chan, J. C. L., Liu, K., Ching, S. E. & Lai, E. S. Asymmetric distribution of convection associated with tropical cyclones making landfall along the South China coast. *Mon. Weather Rev.* **132**, 2410–2420 (2004).
23. Chan, J. C. L. & Liang, X. D. Convective asymmetries associated with tropical cyclone landfall. Part I: f-plane simulations. *J. Atmos. Sci.* **60**, 1560–1576 (2003).
24. Hsu, L.-H., Kuo, H.-C. & Fovell, R. G. On the geographic asymmetry of typhoon translation speed across the mountainous island of Taiwan. *J. Atmos. Sci.* **70**, 1006–1022 (2013).
25. Hsu, L.-H., Su, S.-H., Fovell, R. G. & Kuo, H.-C. On typhoon track deflections near the east coast of Taiwan. *Mon. Weather Rev.* **146**, 1495–1510 (2018).
26. Chan, J. C. L. & Gray, W. M. Tropical cyclone movement and surrounding flow relationships. *Mon. Weather Rev.* **110**, 1354–1374 (1982).
27. Wang, Y. & Holland, G. J. Tropical cyclone motion and evolution in vertical shear. *J. Atmos. Sci.* **53**, 3313–3332 (1996).
28. Au-Yeung, A. Y. & Chan, J. C. L. The effect of a river delta and coastal roughness variation on a landfalling tropical cyclone. *J. Geophys. Res. Atmos.* **115**, D19121 (2010).
29. Tropical cyclone. *World Meteorological Organization (WMO)* <https://wmo.int/topics/tropical-cyclone> (2023).
30. Sajjad, M. & Chan, J. C. L. Risk assessment for the sustainability of coastal communities: a preliminary study. *Sci. Total Environ.* **671**, 339–350 (2019).
31. Sajjad, M. & Chan, J. C. L. Tropical cyclone impacts on cities: a case of Hong Kong. *Front. Built Environ.* **6**, 575534 (2020).
32. Kang, S. K. et al. The North Equatorial Current and rapid intensification of super typhoons. *Nat. Commun.* **15**, 1742 (2024).
33. Lin, Y., Zhao, M. & Zhang, M. Tropical cyclone rainfall area controlled by relative sea surface temperature. *Nat. Commun.* **6**, 6591 (2015).

Publisher's note Springer Nature remains neutral with regard to jurisdictional claims in published maps and institutional affiliations.

Open Access This article is licensed under a Creative Commons Attribution-NonCommercial-NoDerivatives 4.0 International License, which permits any non-commercial use, sharing, distribution and reproduction in any medium or format, as long as you give appropriate credit to the original author(s) and the source, provide a link to the Creative Commons licence, and indicate if you modified the licensed material. You do not have permission under this licence to share adapted material derived from this article or parts of it. The images or other third party material in this article are included in the article's Creative Commons licence, unless indicated otherwise in a credit line to the material. If material is not included in the article's Creative Commons licence and your intended use is not permitted by statutory regulation or exceeds the permitted use, you will need to obtain permission directly from the copyright holder. To view a copy of this licence, visit <http://creativecommons.org/licenses/by-nc-nd/4.0/>.

© The Author(s) 2026

Methods

Selection criteria of landfalling TCs

The International Best Track Archive for Climate Stewardship (IBTrACS, v0400) dataset³⁴ used in this study was obtained from the National Centers for Environmental Information, which contains the motion, track and intensity data of global TCs at 3-hourly intervals, such as TC intensity in terms of maximum wind speed (MWS) and minimum central pressure (MCP), the latitude and longitude of TC location, translation speed, motion direction, nature, landfall condition and distance to land at the current location. Specifically, nature describes the attributes of a TC, including disturbance, tropical system and extratropical system. The 'landfall' provides the minimum distance to land between the current location and the next (usually 3 h) and the 'dist2land' represents the distance to the nearest land point at the current location, both of which can be used to identify the landfalling TCs and to determine the landfall time and location. The IBTrACS dataset includes the global TCs best-track records from multiple agencies in different formats, such as the US National Hurricane Center, Joint Typhoon Warning Center, China Meteorological Administration and the Japan Meteorological Agency. Specifically, records from the World Meteorological Organization (WMO) are used in this study, which contain the position and intensity based on the position(s) and intensities from the various source datasets according to the WMO format. TC intensity is based on the 10-min averaged wind speed at each recorded position.

In this study, the TC best-track records for the period 1950–2021 were used. Only the TCs with landfalling records were selected and the near-landfalling TCs along the coastline were excluded. The selection criteria of landfalling TCs were as follows: (1) only TCs with a lifetime maximum intensity of at least $\geq 17.2 \text{ m s}^{-1}$ (that is, tropical storm intensity) and a lifetimes longer than 60 h. Here, we selected TCs that had been at tropical storm intensity or higher for a substantial period before landfall. We mainly focused on the period within 60 h before landfall because a TC located near to the coastline is likely to be affected by the land during this time and the warning time for a landfalling TC is often ~48–72 h for disaster preparedness. (2) To reduce the influence from irregular tracks, the 'non-main' track types (regular tracks were identified as the 'main' track type in the IBTrACS dataset and other tracks were identified as 'spur' type, indicating that they either merge with or were split from another track (or both) were filtered. Consequently, the selected TCs were already moving steadily towards land. (3) On the basis of the nature of TCs, records of TCs identified as the extratropical transition at the time of landfall were also excluded. With above criteria, a total of 1,803 TCs were selected. (4) For multiple-landfall TCs, the 60 h before the second landfall may already be spent over land. Therefore, this study focused only on the change in translation speed during the 60 h before the first landfall.

After the landfalling TCs were selected, a time series of the average translation speeds of all landfalling TCs at 3-h intervals from 60 h before landfall until the time of landfall was constructed. The average speed was calculated for all coastal areas (Fig. 1a), the two hemispheres (Fig. 1a,b), the six basins (Fig. 1e–j) and other groupings (Extended Data Fig. 1). TCs were divided into four seasons based on their landfall times in the boreal and austral hemispheres, respectively. For TC intensity categories, we used the maximum intensity of TCs during the 60 h before landfall to separate the TCs into six categories according to the Saffir–Simpson Hurricane Wind Scale.

Statistical analysis

The linear trends of translation speed were calculated by the linear regression method and the full degrees of freedom in the time series were used to determine the *P* value of regression coefficients. A two-tailed Student's *t*-test was performed to determine the robustness of the regression trend and whether the mean values of the translation speed between two probability density distributions differ significantly

from each other at the 0.001 confidence level. The percentage change is defined as the ratio of difference between the last and first points of the regression line.

Model configuration

In this study, version 4.0 of the Advanced Research Weather Research and Forecasting (hereafter, WRF) model³⁵ was used to perform an ideal TC numerical experiment. The WRF model is double nested with horizontal resolutions of 10 km (outermost domain: $4,000 \times 4,000$ km) and 5 km (innermost domain: $2,000 \times 2,000$ km) grid spacing, and is configured with 26 vertical levels and the top of the model is set at 25 km. The lateral boundaries of outermost domain are set to be doubly periodic. More details of the model configuration and physical parameterization schemes used in the ideal simulation are provided in Extended Data Table 2 (refs. 36–41).

The model is initialized with a specified analytical vortex at the beginning of the simulation, which can be described as

$$v(r, z, 0)$$

$$= \frac{z_{\text{sponge}} - z}{z_{\text{sponge}}} \left\{ v_m^2 \left(\frac{r}{r_m} \right)^2 \left[\left(\frac{2r_m}{r + r_m} \right)^3 - \left(\frac{2r_m}{r_0 + r_m} \right)^3 \right] + \frac{f^2 r^2}{4} \right\}^{\frac{1}{2}} - \frac{f r}{2}, \quad (1)$$

where r_0 is the outer radius of the vortex at which the tangential wind drops to 0 ($v=0$), v_m and r_m represent the MWS and the radius of maximum wind, respectively, z_{sponge} denotes the upper boundary height above which the wind speed is fully relaxed to zero through a linear decay, f denotes the Coriolis parameter, r is the radial distance from the storm center, and z represents the vertical height.

$$\begin{cases} r_0 = 412,500 \text{ m} \\ r_m = 82,500 \text{ m} \\ v_m = 15 \text{ m s}^{-1} \\ z_{\text{sponge}} = 20,000 \text{ m.} \end{cases} \quad (2)$$

Experimental design

In the model, Jordan's sounding is adopted in the vortex initialization⁴². This is the basic-state potential temperature and humidity in the summertime tropical atmosphere for an approximate representation of real convection. The model is run on an *f*-plane centred at 20°N (Coriolis parameter of $5.0 \times 10^{-5} \text{ s}^{-1}$) and the sea surface temperature remains a constant of 28.5°C throughout the simulation.

To examine the effect of land–sea contrast on the landfalling TC translation speed, an ideal experiment is performed with the combinations of land and sea surfaces, with the domains consisting of a 'rectangular' sea surface and a 'rectangular' land. For the sake of brevity, the north–south-oriented coast with the land use types of dryland, cropland and pasture is 800 km west of the domain centre. The coastline is the boundary between the ocean and the land, with the land in the western side of the domain. In this ideal experiment, the initial vortex with MCP of 1,014 hPa is placed in the domain centre embedded in an easterly flow from the surface to the top of model and it is horizontally homogeneous. So as not to create a large wind asymmetry across the vortex, we only impose a weak 1 m s^{-1} easterly steering flow ($u = -1 \text{ m s}^{-1}$, $v = 0 \text{ m s}^{-1}$) onto the vortex to push the vortex towards the land west of the vortex.

The ideal simulation is run for 240 h. As the main interest here focuses on the effect of land–sea contrast on the landfalling TC movement, the model outputs from the 60 h period before TC making landfall to the landfall time are extracted. The TC track is determined from the surface pressure centre and the translation speed is calculated using the time-centred difference of TC positions. Correspondingly, the MCP at the surface and 10-m MWS are used to represent the TC

intensity. It can be seen from Fig. 2a,b that the average speed of the simulated TC increases as it approaches the land. During this period, the MSW of the simulated TC changes from approximately 57 m s^{-1} to a peak intensity of 60 m s^{-1} and then gradually weakens to around 43.48 m s^{-1} . The MCP of the simulated TC undergoes a change from -960 to -985 hPa , with a peak intensity of 956.20 hPa (Fig. 2c,d).

To mitigate the random effects of case studies (for example, diurnal variation) on the change in translation speed of TCs, we also conducted a set of ensemble simulations under different steering flows. The ensemble-averaged translation speed of TCs exhibits acceleration when they are within 700 km of land. However, when located approximately 100 km from land, the ensemble-averaged translation speed continues to increase but the rate of acceleration slightly decreases (Extended Data Fig. 8a). This phenomenon is probably linked to the rapid weakening of TC intensity (Extended Data Fig. 8b), which causes changes in the structure of PV and PVT as the TCs approach landfall.

Moreover, the output variables in the model eta level are interpolated to height levels, and the TC centre location is defined as the position of MCP at the various height levels, which would be used to calculate the PV and its PVT.

PVT method

Given that a TC is often regarded as an area of positive PV and its motion refers as the propagation of the PV anomaly, the PVT method was introduced to diagnose the effects of different physical processes on TC motion^{15,20,21}. The PV tendency is computed as

$$\left(\frac{\partial P}{\partial t} \right)_{1m} = \left(\frac{\partial P}{\partial t} \right)_{1f} + \vec{C} \cdot \nabla P_s, \quad (3)$$

where subscript 1 denotes the azimuthal wavenumber-one component of the PVT and subscripts m and f denote the moving and fixed reference frames relative to the TC centre, respectively, ∇ is the Hamilton operator, \vec{C} is the PVT speed of the TC, and P_s is the symmetric component of PV (refers to the wavenumber-zero component) with respect to the TC centre. For a given 2D variable field $F(r, \theta)$ (for example, PV field), each wavenumber component of the variable field $F_k(r)$ is calculated by using the Fourier transform, which is given as

$$F_k(r) = \frac{1}{2\pi} \int_0^{2\pi} F(r, \theta) e^{-ik\theta} d\theta, \quad (4)$$

where r and θ represent the radial distance and azimuthal angle, respectively, and π is a mathematical constant defined as the ratio of a circle's circumference to its diameter. The 2D variable field at the various height levels is projected as a function of the radial distance at 10° -Kim intervals and the azimuth at 10° intervals relative to the storm centre at the corresponding level, and the maximum radius of circle is set to 120 km . Note that the results are insensitive to the choice of radius as it is able to cover the inner-core structure of the TC and because the PVT speed is determined by the gradient of the symmetric component of PV. Then, the discrete fast Fourier transform is used to extract the various azimuthal wavenumber components of the different variable fields at all height levels. The results of the wavenumber analysis are insensitive to the choice of interval for the radial distance and azimuth, and the maximum radius distance since the PVT translation speed is determined by the gradient of symmetric component of PV. The local change rate term (that is, PV tendency) and gradient term of each variable (for example, the gradient of symmetric PV) are calculated with the centred finite difference method. The least squares method is used to estimate the PVT speed. For more details of the algorithm and steps, refer to ref. 15.

In this study, the PVT method is used to examine the effects of land surface on the acceleration motion of TC. To quantitatively identify the

relative contribution of various physical processes to the TC motion, such as the effect of HA, VA and DH, the PVT equation in the fixed reference is written as

$$\left(\frac{\partial P}{\partial t} \right)_{1f} = \Lambda_1 (-\mathbf{V}_h \cdot \nabla_h P - w \frac{\partial P}{\partial z} + \frac{\vec{\eta}}{\rho} \cdot \nabla \frac{d\theta_v}{dt} + R), \quad (5)$$

where P , \mathbf{V}_h , w and θ_v represent the PV, horizontal wind vector, vertical velocity and virtual potential temperature, respectively. The operator Λ_1 denotes the calculation of the wavenumber-one component using the Fourier transform, which is similar to equation (4). The $\vec{\eta}$ is the absolute vorticity and ρ represents the total air density. $(\frac{\partial P}{\partial t})_{1f}$ is the wavenumber-one component of the PV tendency in the fixed reference frames, which is the sum of the HA $-\mathbf{V}_h \cdot \nabla_h P$, VA $-w \frac{\partial P}{\partial z}$ and DH $\frac{\vec{\eta}}{\rho} \cdot \nabla \frac{d\theta_v}{dt}$ terms and residual term R . The residual term consists of the friction term and the effects related to momentum flux.

To further determine the individual contributions, the HA term can be split into two terms to represent the steering flow and the asymmetric flow, namely the AASPV and the SAAPV²², which are given as

$$-\mathbf{V}_h \cdot \nabla_h P = -\mathbf{V}_1 \cdot \nabla P_s - \mathbf{V}_s \cdot \nabla P_1, \quad (6)$$

where \mathbf{V}_s and P_s represent the symmetric components (s refers to the wavenumber-zero components) respectively of the wind speed and PV with respect to the TC centre. Similarly, \mathbf{V}_1 and P_1 are their asymmetric components (1 refers to the wavenumber-one component). The higher-order terms are neglected.

The DH term $\frac{\vec{\eta}}{\rho} \cdot \nabla \frac{d\theta_v}{dt}$ is also split into three terms to represent the different components of heating gradient, which can be written as

$$DH = \frac{1}{\rho} \left[\left(\frac{\partial w}{\partial y} - \frac{\partial v}{\partial z} \right) \frac{\partial \theta_v}{\partial x} + \left(\frac{\partial u}{\partial z} - \frac{\partial w}{\partial x} \right) \frac{\partial \theta_v}{\partial y} + (\xi + f) \frac{\partial \theta_v}{\partial z} \right], \quad (7)$$

where u and v represent the horizontal components of wind speed, w is the vertical velocity, ξ the relative vorticity and f denotes the Coriolis parameter of $5.0 \times 10^{-5} \text{ s}^{-1}$ (corresponding to an f -plane at 20°N). The first two terms on the right-hand side represent the coupling between vertical wind shear, horizontal gradient of vertical motion and that of heating, similar to the tilting term in the barotropic vorticity equation. The last term on the right-hand side is the coupling between absolute vorticity and the vertical variation of heating, similar to the divergence term in the barotropic vorticity equation. As these three terms are all related to the gradients of heating in the three directions, they will be labelled as DH-X, DH-Y and DH-Z, respectively.

Data availability

The International Best Track Archive for Climate Stewardship (IBTrACS v0400) dataset is publicly available from the National Centers for Environmental Information (<https://www.ncei.noaa.gov/products/international-best-track-archive>). The processed source data used to perform the analyses and generate all figures are available via Zenodo at <https://doi.org/10.5281/zenodo.17020964> (ref. 43). The original model output data are too large to be uploaded to a public repository and are available from the corresponding authors upon request.

Code availability

The data analysis and visualization were performed using the NCAR Command Language⁴⁴. In particular, the diagnostic analysis follows the procedures described in Methods and relies on customized scripts that involve multiple function libraries and complex workflows. As these codes cannot be packaged into a stable and publicly shareable form, they are available from the first author (Q.Z., email: zqj@lasg.iap.ac.cn) upon request.

References

34. Knapp, K. R., Kruk, M. C., Levinson, D. H., Diamond, H. J. & Neumann, C. J. The International Best Track Archive for Climate Stewardship (IBTrACS) unifying tropical cyclone data. *Bull. Am. Meteorol. Soc.* **91**, 363–376 (2010).
35. Skamarock, W. C. et al. *A Description of the Advanced Research WRF Version 3 NCAR Technical Note-475+STR 1-113* (National Center for Atmospheric Research, 2008).
36. Hong, S.-Y. & Pan, H.-L. Nonlocal boundary layer vertical diffusion in a medium-range forecast model. *Mon. Weather Rev.* **124**, 2322–2339 (1996).
37. Dudhia, J. et al. Prediction of Atlantic tropical cyclones with the Advanced Hurricane WRF (AHW) model. In *Proc. 28th Conference on Hurricanes and Tropical Meteorology* (American Meteorological Society, 2008).
38. Hong, S.-Y. & Lim, J.-O. J. The WRF single-moment 6-class microphysics scheme (WSM6). *Asia-Pac. J. Atmos. Sci.* **42**, 129–151 (2006).
39. Kain, J. S. The Kain-Fritsch convective parameterization: an update. *J. Appl. Meteor. Climatol.* **43**, 170–181 (2004).
40. Lacis, A. A. & Hansen, J. A parameterization for the absorption of solar radiation in the earth's atmosphere. *J. Atmos. Sci.* **31**, 118–133 (1974).
41. Schwarzkopf, M. D. & Fels, S. B. The simplified exchange method revisited: an accurate, rapid method for computation of infrared cooling rates and fluxes. *J. Geophys. Res. Atmos.* **96**, 9075–9096 (1991).
42. Jordan, E. S. Mean soundings for the West Indies area. *J. Atmos. Sci.* **9**, 91–97 (1958).
43. Zhong, Q. Landfalling tropical cyclones accelerate due to land-sea thermal and roughness contrasts (source data). *Zenodo* <https://doi.org/10.5281/zenodo.17020964> (2025).
44. The NCAR Command Language (version 6.6.2). UCAR/NCAR/ CISL/TDD <https://doi.org/10.5065/D6WD3XH5> (2019).

Acknowledgements

This research was jointly supported by the National Natural Science Foundation of China (grant nos 42225501 (to R.D.), 42105059 (to Q.Z.)

and 722293604 (to S.T.)), the Fundamental Research Funds for the Central Universities (grant no. 2243300004 (R.D.)) and the Center for Ocean Research in Hong Kong and Macau (CORE). CORE is a joint ocean research centre between the Laoshan National Laboratory for Marine Science and Technology and the Hong Kong University of Science and Technology. We thank H. Yang and Y. Feng from L. Wu's group at Fudan University for their assistance in the PVT calculation.

Author contributions

Q.Z. conducted the data analyses and designed the numerical experiment. Q.Z. and J.C.L.C. conceived the idea and co-wrote the paper together with R.D. The other authors contributed to the discussion and interpretation of the results.

Competing interests

The authors declare no competing interests.

Additional information

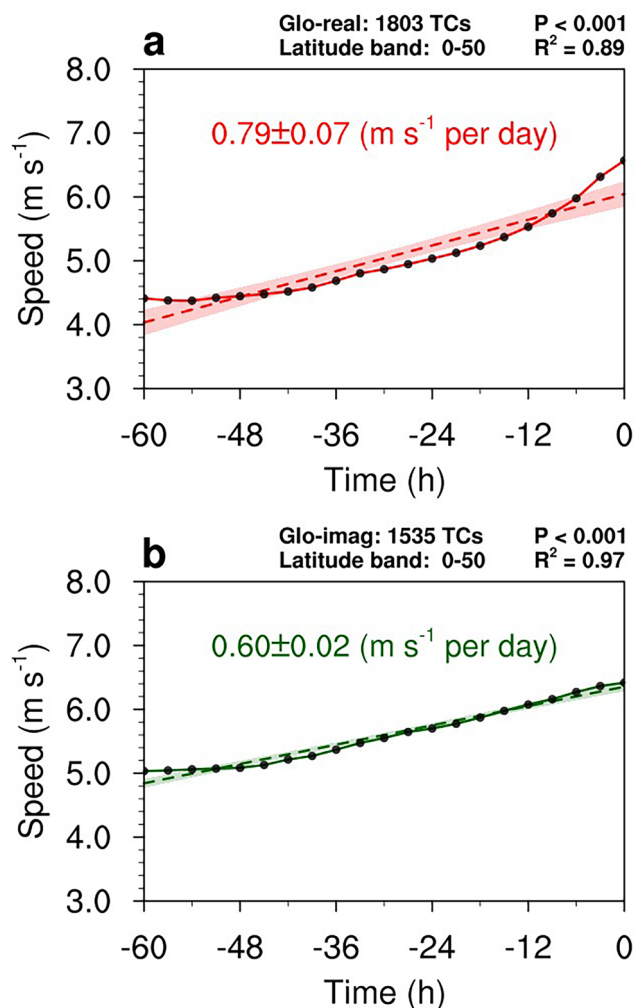
Extended data is available for this paper at <https://doi.org/10.1038/s41561-025-01891-1>.

Supplementary information The online version contains supplementary material available at <https://doi.org/10.1038/s41561-025-01891-1>.

Correspondence and requests for materials should be addressed to Johnny C. L. Chan or Ruiqiang Ding.

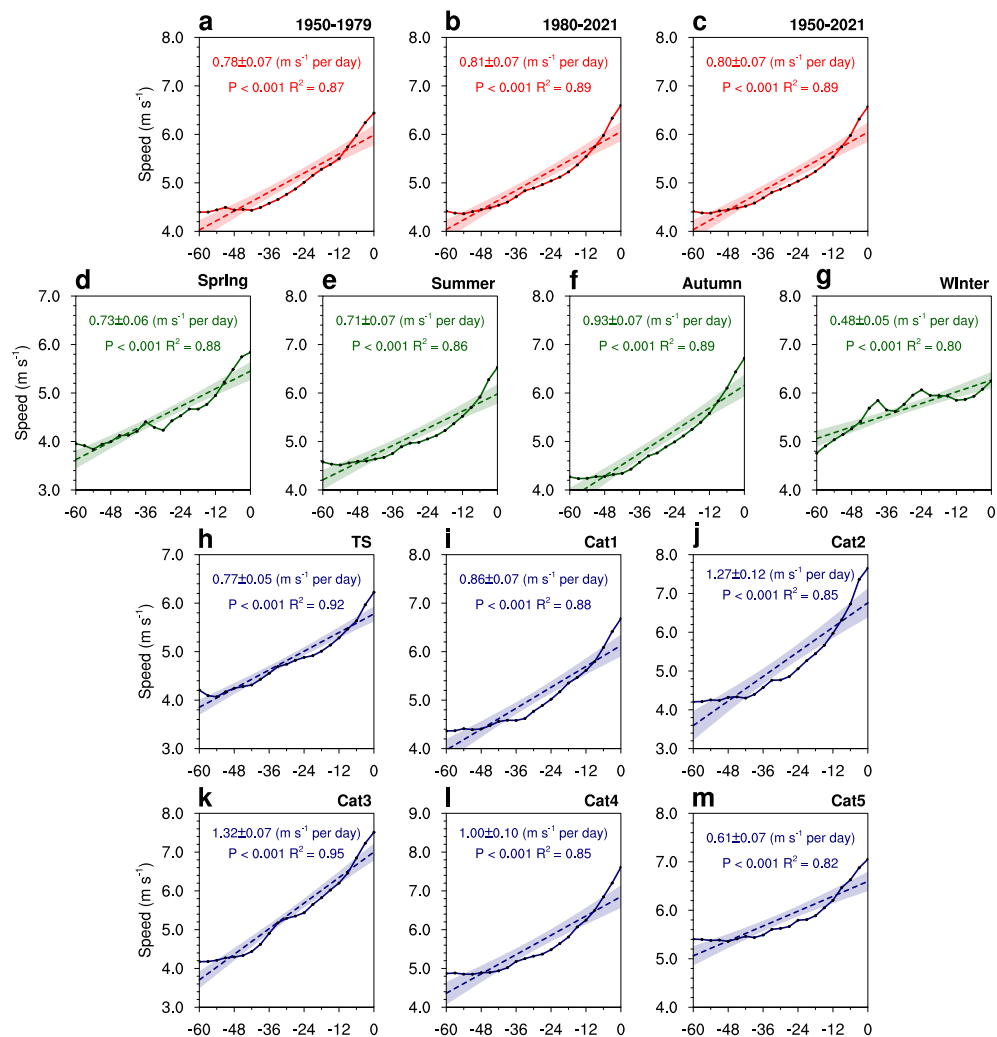
Peer review information *Nature Geoscience* thanks Chris Landsea, Ralf Toumi and Jill Trepanier and the other, anonymous, reviewer(s) for their contribution to the peer review of this work. Primary Handling Editors: James Super and Thomas Richardson, in collaboration with the *Nature Geoscience* team.

Reprints and permissions information is available at www.nature.com/reprints.



Extended Data Fig. 1 | Changes in the mean translation speed of landfalling and non-landfalling tropical cyclones (TCs) and their trends. Panels show mean translation speed of TCs in all ocean basins: **a** landfalling TCs, and **b** non-landfalling TCs at the same latitude ranges. Landfalling TCs cross the actual coastline, while non-landfalling TCs are from a random sample crossing an

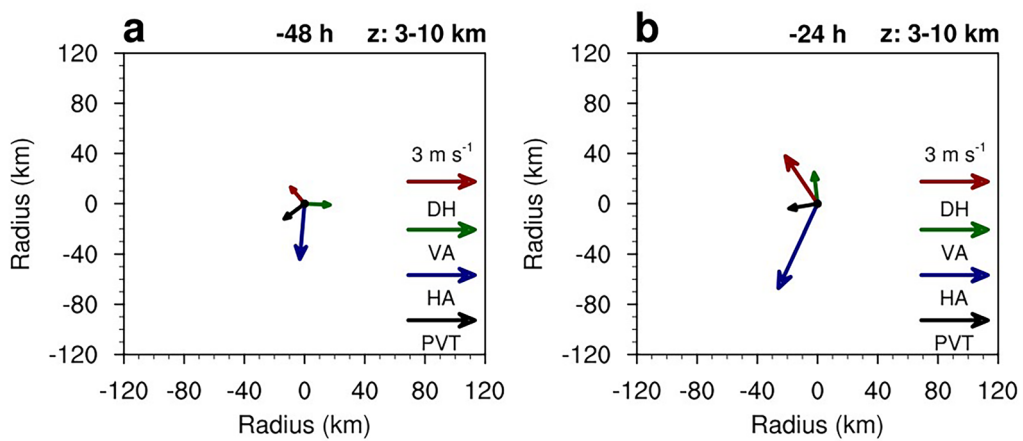
imaginary coastline 800 km offshore. Dashed lines denote the linear trend, and shading indicates the two-sided 95% confidence intervals of the trend based on a Student's t-test. The linear regression coefficients with their standard errors ($\text{m s}^{-1} \text{ per day}$) are shown at the top center, and the corresponding R^2 and P values are shown at the top of each panel.


Extended Data Fig. 2 | Changes in the mean translation speed of landfalling

TCs 60 h before landfall and their trends. Mean translation speed 60 h before landfall is shown for different periods: **a** 1950–1979 (pre-satellite era),

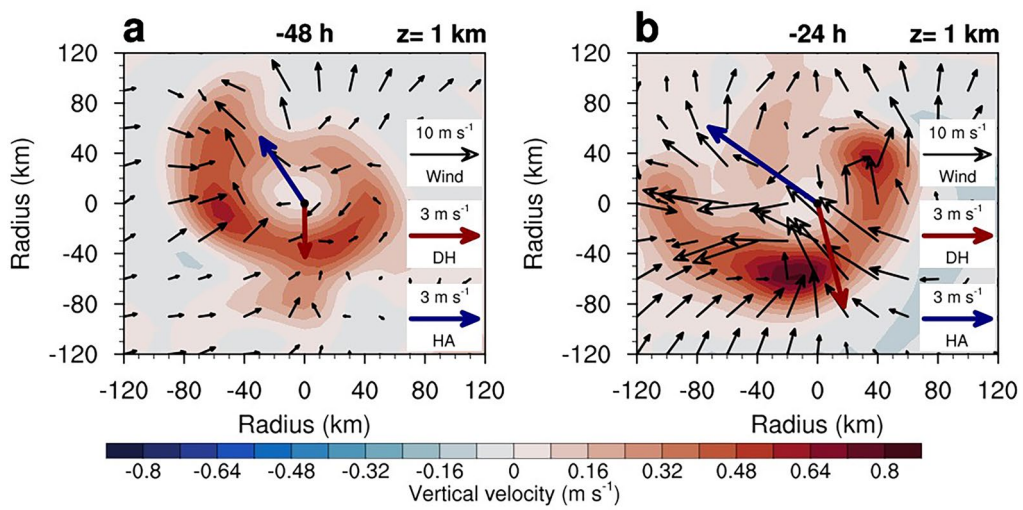
b 1980–2021 (post-satellite era), and **c** 1950–2021. Seasonal variations: **d** spring, **e** summer, **f** autumn, **g** winter. Intensity categories: **h** TS, **i** Cat1, **j** Cat2, **k** Cat3,

l Cat4, **m** Cat5. Dashed lines denote the linear trend, and shading indicates the two-sided 95% confidence intervals of the trend based on a Student's t-test. The linear regression coefficients with their standard errors (m s⁻¹ per day), together with the corresponding R² and P values, are shown at the top center of each panel.



Extended Data Fig. 3 | Potential vorticity tendency (PVT) vector and its various components. Potential vorticity tendency (PVT) speed (black) averaged from 3 to 10 km altitude and its contributions from the horizontal advection (HA,

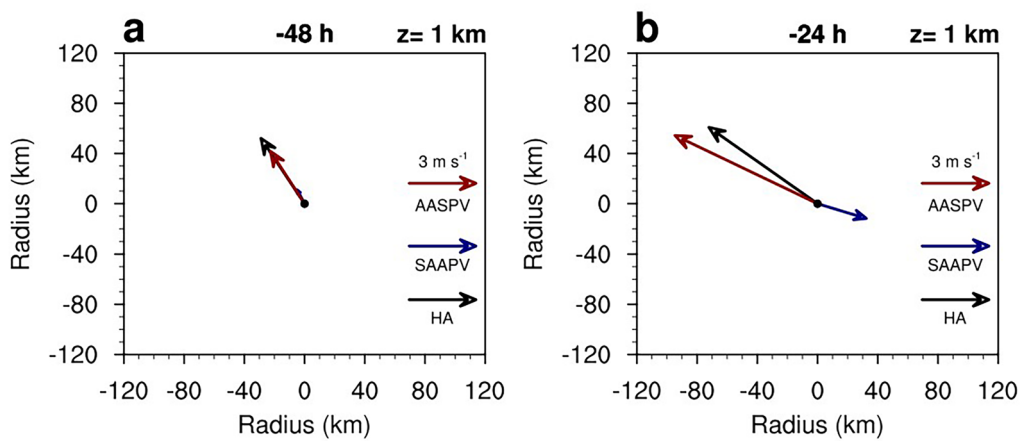
blue), vertical advection (VA, green) and diabatic heating (DH, red) terms at **a**. 48 h prior to landfall (-48 h) and **b**. 24 h prior to landfall (-24 h). The magnitude of the reference vector is 3 m s^{-1} .



Extended Data Fig. 4 | Distribution of asymmetric wind flow and vertical velocity of the simulated tropical cyclone (TC) over time at 1 km height.

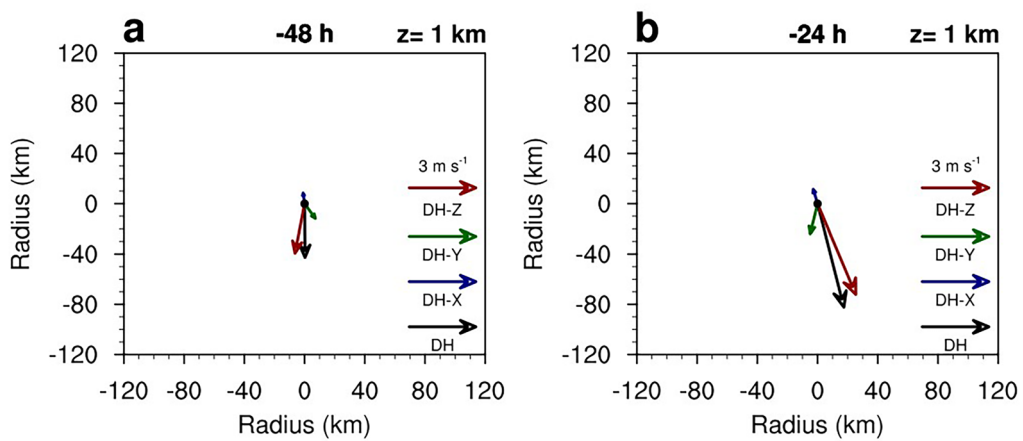
a –48 h, **b** –24 h. The black arrows and the shading represent the asymmetric wind

vectors and the vertical velocity, respectively. The thick blue and red arrows are the contributions of horizontal advection (HA) and diabatic heating (DH) to the potential vorticity tendency (PVT) vector. The black dot represents the TC center.



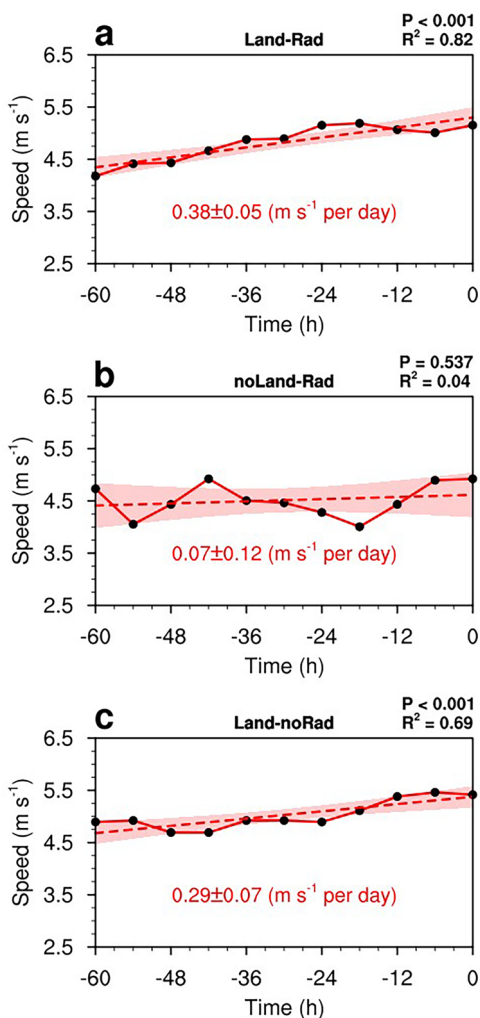
Extended Data Fig. 5 | The contribution of horizontal advection (HA) to potential vorticity tendency (PVT) speed and its various components of the simulated tropical cyclone (TC) over time at 1 km height. a -48 h, **b** -24 h. The contribution of HA (black) to the PVT speed and its variations of contributions

from the asymmetric advection of symmetric PV (AASPV, red) and the symmetric advection of asymmetric PV (SAAPV, blue) terms. The black dot represents the TC center.



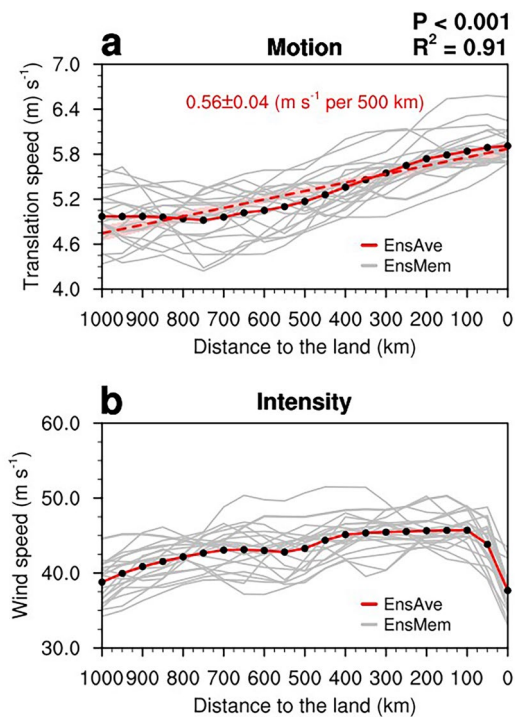
Extended Data Fig. 6 | The contribution of diabatic heating (DH) to the potential vorticity tendency (PVT) speed and its various components of the simulated tropical cyclone (TC) over time at 1 km height. a –48 h, b –24 h.

The contributions of DH (black) to the PVT vector and its variations of contributions from x- (DH-X, blue), y- (DH-Y, green) and z- (DH-Z, red) components of the heating gradient, respectively. The black dot represents the TC center.



Extended Data Fig. 7 | Translation speed of a simulated TC under a 5 m s^{-1} steering flow. **a** Simulation with land and radiation (Land-Rad), **b** simulation without land but with radiation (noLand-Rad), and **c** simulation with land but without radiation (Land-noRad). Dashed lines denote the linear trend, and

shading indicates the two-sided 95% confidence intervals of the trend based on a Student's t-test. The linear regression coefficients with their standard errors (m s^{-1} per day) are shown at the bottom center, and the corresponding R^2 and P values are shown at the top right of each panel.



Extended Data Fig. 8 | Ensemble simulations. Ensemble simulations of TC motion (a) and intensity (b) as a function of distance to land. The gray solid lines represent the ensemble members (EnsMem), while the red solid and dashed lines represent the ensemble average (EnsAve) and its linear trend (dashed line), respectively. Dashed lines denote the linear trend, and shading indicates the

two-sided 95% confidence intervals of the trend based on a Student's t-test. The linear regression coefficients with their standard errors (m s^{-1} per day) are shown at the bottom center, and the corresponding R^2 and P values are shown at the top right of panel.

Extended Data Table 1 | Statistics of tropical cyclones (TCs) translation speed with time for various hemispheres, periods, seasons, basins, and TC intensities

	Number of TCs	Mean speed (m s ⁻¹)	Trend (m s ⁻¹ per day)
Global	1803	5.03	0.79±0.07
N. Hemisphere	1367	5.31	0.86±0.07
S. Hemisphere	436	4.16	0.62±0.05
Pre-satellite era (1950-1979)	339	5.01	0.78±0.07
Post-satellite era (1980-2021)	1464	5.05	0.81±0.07
WP	669	5.68	1.00±0.08
EP	180	4.39	0.75±0.10
NA	420	5.33	0.74±0.06
SP	201	4.35	0.71±0.08
NI	98	4.29	0.84±0.05
SI	233	4.02	0.54±0.04
Spring	88	4.54	0.73±0.06
Summer	845	5.09	0.71±0.06
Autumn	810	4.99	0.93±0.07
Winter	60	5.66	0.48±0.05
TS	644	4.82	0.77±0.05
Cat1	275	5.05	0.86±0.07
Cat2	156	5.18	1.27±0.12
Cat3	115	5.35	1.32±0.07
Cat4	185	5.61	1.00±0.10
Cat5	79	5.83	0.61±0.07
Idealized TC	1	1.56	0.21±0.03

'P-value' represents the significance of these linear trends, and 'Increment' represents the differences in average translation speed between the first and last points of the linear trend. The p values for all groups are < 0.001. The trend and increment are calculated globally, in the two hemispheres [(NH: Northern Hemisphere, SH: Southern Hemisphere)], in the three periods [1950-1979 (pre-satellite era), 1980-2021 (post-satellite era) and 1950-2021], in individual basins [(WNP: western North Pacific, ENP: eastern North Pacific, NA: North Atlantic, SI: South Indian Ocean, SP: South Pacific, NI: North Indian Ocean)], in the four seasons (that is, spring, summer, autumn, and winter), and with different TC intensities (that is, TS: tropical storm, Cat1: category 1, Cat2: category 2, Cat3: category 3, Cat4: category 4, and Cat5: category 5). Mean speed is calculated for each grouping of TCs from 60 h before landfall to landfall.

Extended Data Table 2 | Model details and physical parameterization schemes

Model version	WRF-ARW Version 4.0	
Domain	D01	D02
Resolution	10 km	5 km
Horizontal grid size	4000 × 4000 km	2000 × 2000 km
Grid number	400 × 400	
Time step	40 seconds	
Integration period	0–240 h (Output: 6 h intervals)	
Coriolis parameter (f-plane)	$5.0 \times 10^{-5} \text{ s}^{-1}$	
SST	28.5 °C	
Planetary boundary layer	Yonsei University (YSU) boundary layer scheme ³⁶	
Surface layer	Surface layer scheme of Dudhia et al. ³⁷	
Microphysics	WRF single-moment six-class (WSM6) microphysics ³⁸	
Cumulus	Kain-Fritsch (new Eta) scheme ³⁹	Not used
Radiation	RRTMG Shortwave/Longwave Radiation Scheme ^{40,41}	
Vertical η -level	26 levels (model top is set to 25 km)	